



Repositorio Institucional de la Universidad Autónoma de Madrid

<https://repositorio.uam.es>

Esta es la **versión de autor** del artículo publicado en:
This is an **author produced version** of a paper published in:

Applied Catalysis B: Environmental 246, (2019): 1-11

DOI: <https://doi.org/10.1016/j.apcatb.2019.01.054>

Copyright: © 2019 Elsevier B.V. All rights reserved.

El acceso a la versión del editor puede requerir la suscripción del recurso

Access to the published version may require subscription

INFLUENCE OF TiO₂-rGO OPTICAL PROPERTIES ON THE PHOTOCATALYTIC ACTIVITY AND EFFICIENCY TO PHOTODEGRADE AN EMERGING POLLUTANT

Álvaro Tolosana-Moranchel^{1*}, Agustina Manassero², María L. Satuf², Orlando M. Alfano², José A. Casas¹, Ana Bahamonde³

¹Departamento de Ingeniería Química, Facultad de Ciencias, C/ Francisco Tomás y Valiente 7, Universidad Autónoma de Madrid, 28049 Madrid (Spain).

²Instituto de Desarrollo Tecnológico para la Industria Química (Universidad Nacional del Litoral and Consejo Nacional de Investigaciones Científicas y Técnicas), predio CONICET “Dr. Alberto Cassano”, Ruta Nacional N°168, 3000 Santa Fe, Argentina.

³Instituto de Catálisis y Petroleoquímica, ICP-CSIC, C/ Marie Curie 2, 28049 Madrid (Spain).

ABSTRACT

TiO₂-reduced graphene oxide (TiO₂-rGO) photocatalysts with different mass ratios (GO:TiO₂ 0.1-0.5-1%) were synthesized via a hydrothermal method and compared through their physico-chemical properties and photocatalytic activity in the degradation of an emerging contaminant, clofibric acid. The optical properties of the TiO₂-rGO nanocomposites were first estimated in order to calculate the local volumetric rate of photon absorption inside a photocatalytic reactor. Radiation models were solved using the Monte Carlo method. The effect of rGO as well as the photocatalyst loadings on the radiation absorption was evaluated. The lowest photodegradation rate found in P25-rGO 1% was ascribed to an excess of rGO that could well favor charge carriers recombination leading to detrimental photoactivity. A GO/TiO₂ mass ratio of 0.5 % provided the fastest initial photodegradation rate under the operating conditions studied here. Finally, the photo-efficiency of all these photocatalysts was also analyzed by calculating the quantum efficiency parameter. The highest value of quantum efficiency was achieved with P25-rGO 0.5% at 100 mg L⁻¹, with an increase of 11% compared to the value obtained for P25-rGO 0%.

Keywords: photocatalysis, TiO₂-rGO, Monte Carlo, optical properties, Clofibric acid

*Corresponding author. e-mail address: alvaro.tolosana@uam.es

1. INTRODUCTION

Over the last decades, the ubiquitous presence of pharmaceutical compounds, considered as emerging contaminants (ECs), has increasingly become a matter for concern. These type of pollutants are being detected in drinking water, groundwater and surface water at concentrations ranging from $\text{ng}\cdot\text{L}^{-1}$ to $\text{mg}\cdot\text{L}^{-1}$ [1, 2]. Even at these concentrations, they can pose a threat to aquatic environments and human health [1, 3, 4]. Sources of water contamination with ECs are sewage effluents from domestic and industrial facilities and industrial effluent discharges. Since conventional municipal (MWWTP) or industrial wastewater treatment plants (WWTP) were not designed to eliminate these compounds, low removal efficiency is achieved [5-7]. Pharmaceuticals can also be spread by applying the sewage sludge as a fertilizer or by landfill leakage favoring their ubiquity in groundwater [1-3]. Therefore, tertiary treatments are necessary to be implemented in WWTP to prevent the release of ECs into the natural waters [2, 5, 6, 8, 9].

In this context, advanced oxidation processes (AOPs), in which hydroxyl radicals (HO^\bullet) are generated, have been widely investigated to remove water pollutants [2, 6, 10]. Among them, heterogeneous photocatalysis has received a lot of attention to degrade ECs. This process is based on the use of a semiconductor with wide band gap that involves the generation of electron-hole pairs when the semiconductor is irradiated with sufficiently energetic light (usually UV light). Electrons are promoted to the conduction band where they can react with oxygen to form oxidizing species such as superoxide radical anions ($\text{O}_2^{\bullet-}$). Valence band holes can either directly oxidize an organic compound adsorbed on the catalyst surface or react with adsorbed water molecules to generate HO^\bullet radicals that further oxidize the pollutant [10-12]. Previous research on the use of photocatalysis to degrade pharmaceuticals has shown good results [2, 13, 14]. One of the most investigated semiconductors is TiO_2 because of its useful properties: resistance to chemical corrosion and photo-corrosion, high activity, cost-effectiveness and non-toxicity [10, 15]. However, photocatalysis has some limitations that need to be solved prior to its commercial application: firstly, TiO_2 photocatalysts are only able to harvest photons from UV radiation leading to low efficiencies when solar light is employed; and secondly, more accurate procedures to design and scale-up photocatalytic reactors are necessary [15-19].

Because of the ineffective utilization of visible light by TiO_2 and short lifetime of photogenerated charge carriers, new photocatalysts are being recently designed to overcome these limitations [11, 20]. Among them, carbon-based TiO_2 composites have been reported to reduce electron-hole recombination. However, in recent years, semiconductor-graphene has been widely investigated owing to the unique properties of graphene: good optical and thermal transmittance, chemical stability, large area, and high charge carrier mobility [20, 21]. In this context, one of the most widely used techniques to synthesize TiO_2 -

graphene and TiO₂-reduced graphene oxide (rGO) nanocomposites is via a hydrothermal method [13, 22-24]. Several studies have reported higher photocatalytic activity of these nanocomposites compared to pristine TiO₂ [13, 24-26]. The main advantages of the TiO₂-rGO junction are ascribed to a decrease of its band gap, which makes possible to harvest visible light, an increase in the specific surface area, and a reduction in the electron-hole recombination, since electrons can be transferred from the TiO₂ conduction band to the reduced graphene oxide [20, 21, 27]. Thanks to these advantages Alamelu et al. [28] reported that TiO₂-graphene nanocomposites were able to increase organic dyes photodegradation by a factor between 3.5 and 15 compared to bare TiO₂. Similarly, Wu et al. [29] synthesized highly stable TiO₂-rGO photocatalysts. These photocatalysts proved to be effective to photodegrade organic dyes because of its stability, its charge separation efficiency and the high surface area of rGO. Furthermore, TiO₂-rGO photocatalysts have also been reported to improve antibacterial activity increasing sterilization rates by 1.4 times compared to the bare coating [30]. In this case, the improvement was ascribed to a higher hydroxyl radical formation rate. These nanocomposites have also been used to degrade pollutants from air. Wang et al. [31] reported that TiO₂-graphene exhibited higher photocatalytic activity (1.7 times higher than bare TiO₂) in acetone photodegradation in air. The integration of graphene allowed retarding electron-hole recombination and lead to a more effective electron transfer. On the other hand, new photocatalysts, such as ternary nanocomposites, were synthesized to achieve visible absorption and high photoactivity. A Ag₂CrO₄/g-C₃N₄/graphene oxide (GO) nanocomposite was used to photoreduce CO₂ [32]. Thanks to the matched band structure, the ternary nanocomposite follows a Z-scheme mechanism which enhanced CO₂-conversion. This system showed improved light absorption, charge separation and higher amount of active sites provided by GO. However, to objectively compare the performance of the photocatalysts synthesized by different research groups in different experimental setups, it is useful to relate the photocatalytic activity to the radiation absorbed by the photocatalyst since photo-activation is the first step of the process. Therefore, the development of accurate models to describe radiation absorption has received a great deal of attention [17-19, 33-40]. Firstly, in order to estimate the photons absorbed by the photocatalyst, information about the optical properties of the catalyst suspension is required: absorption and scattering coefficients, and phase function for scattering [18, 41, 42]. This information is further used to solve the radiative transfer equation (RTE) inside the photoreactor to calculate the local volumetric rate of photon absorption (LVRPA). Several methods can be employed to solve the RTE. Among the most frequently used, we found the discrete ordinate method (DOM), the Monte Carlo method, and the “two-flux” or “six-flux” radiation absorption-scattering models [17, 18, 38]. Over the last few years, the Monte Carlo method has been increasingly employed because of its accuracy and its

simple application to model reactors with complex geometries and under uneven irradiation conditions [17, 19, 40, 43]. Furthermore, only intrinsic kinetic models with an explicit dependence on the photon absorption rate are suitable to obtain predictive results independent of the experimental set up and, therefore, useful for the design and scaling-up of photoreactors [17, 18, 35, 38, 44]. Thus, the knowledge of the optical properties is a key feature to calculate the photons absorbed by photocatalysts and, therefore, to determine the final efficiency of the photocatalytic process.

The main novelty of this work is the estimation of the optical properties of several hydrothermally prepared TiO₂-rGO nanocomposites, with different GO doping ratios, and the evaluation of their activity in the photocatalytic degradation of clofibric acid, selected as model pollutant of ECs. Clofibric acid is the active metabolite of a pharmaceutical used as blood lipid regulator whose intermediates and degradation pathways have already been reported [14, 45]. The influence of the presence of rGO and the photocatalyst concentration on the radiation absorption inside the reactor was evaluated by solving a radiation model using the Monte Carlo method. Finally, a comparison study of the photocatalytic performance of the TiO₂-rGO nanocomposites was carried out by calculating the quantum efficiency parameter which relates moles of pollutant removed to moles of photons absorbed by photocatalyst in the reaction medium.

2. EXPERIMENTAL SECTION

2.1. Chemicals

Graphene oxide (GO) water dispersions (0.4 wt% concentration) and titanium dioxide P25 Aeroxide® (80:20 anatase-rutile, BET specific surface area 54 m² g⁻¹, average anatase and rutile crystal size of 21 and 33 nm, respectively) were provided by Graphenea and Evonik Company, respectively. Clofibric acid (CA>97%) was purchased from Aldrich. 4-Chlorophenol (4-CP>99%) and p-benzoquinone (p-BQ>98%) were obtained from Aldrich and Fluka, respectively. All reagents were employed without further treatment and ultrapure water was used to prepare all the solutions.

2.2. Synthesis of P25-rGO

Titanium dioxide P25-rGO composites (P25-rGO) were prepared by a hydrothermal method. Briefly, 2 g of TiO₂ P25 were suspended in 400 mL of ultrapure water and stirred for 30 min at 500 rpm. Then, the desired amount of GO was added and the suspension was further stirred for 2.5 h to achieve a good dispersion of GO sheets. The mixture was then transferred to a 600-mL Teflon-lined stainless steel autoclave reactor and subjected to hydrothermal treatment for 3 h at 120 °C. Afterward, the composite was washed and centrifuged 3 times,

and finally dried at 50 °C. The weight ratios GO:P25 were 0, 0.1, 0.5 and 1%, denoted as P25-rGO 0%, P25-rGO 0.1%, P25-rGO 0.5% and P25-rGO 1%, respectively.

2.3. Photocatalyst characterization

Band gap and UV-visible absorption properties of the photocatalysts were studied after recording their diffuse reflectance spectra with a UV-Visible Agilent-Varian, Cary 5000, equipped with an integrating sphere. The equation $(\alpha \cdot h \cdot \nu)^{1/2} = A \cdot (h\nu - E_g)$ was used to obtain the band gap values of the samples, where α is the absorption coefficient of the solid photocatalyst [46]. A Renishaw Micro Raman spectrometer ($\lambda = 532$ nm) equipped with a 20 mW He-Ne laser emitting at 532 nm was used to obtain the Raman spectra of the samples. Spectra were recorded using 5 repetitions, 10 seconds of acquisition time and 0.2 mW of incident power. Energy Dispersive X-Ray Analysis (EDX) was performed on a Hitachi S-3000N electron microscope equipped with Oxford Instruments INCA x-sight. To study structure and morphology of the TiO₂-based materials, scanning electron microscopy (SEM) analyses and transmission electron microscope (TEM) studies were carried out using a Philips XL 30 S-FEG and a field emission gun JEOL 2100F microscope operating at 200KV, respectively. Samples for TEM were prepared by dry deposition of the composites in a lacey carbon copper grid. Crystal structure of the photocatalysts were analyzed with a X-ray polycrystal PANalytical X'Pert PRO using nickel-filtered Cu K α (1.541874 Å) radiation operating at 40 kV and 40 mA, with a 0.02° step size and accumulating a total of 50 s per point. Crystallite sizes were estimated by employing the Scherrer equation [47] and the crystalline phases were identified by comparison with ICDD PDF database [48]. The specific surface areas were determined by the Brunauer-Emmett-Teller (BET) method [49] from N₂ isotherm data measured at 77 K in a Micromeritics ASAP 2420 apparatus on samples previously outgassed overnight at 413 K to a vacuum of <10⁻⁴ Pa to ensure a dry, clean surface.

2.4. Measurement of optical properties

Extinctance, diffuse transmittance and diffuse reflectance measurements of the P25-rGO composites suspensions were carried out in an Optronic OL series 750 spectroradiometer. For diffuse measurements, an OL 740-70 integrating sphere reflectance attachment was used. All measurements were carried out in the range between 315 and 415 nm. The path length of the measuring rectangular quartz cuvette was 2 mm. Suspensions with photocatalyst concentrations of 50, 100, 250 and 400 mg·L⁻¹ in distilled water were prepared and sonicated for 30 minutes prior to the measurements.

2.5. Photocatalytic experiments

Photocatalytic degradation experiments were carried out in a stainless steel reactor with an inner Teflon wall. The reactor geometry was cylindrical with two circular windows made of borosilicate glass (reactor length: 2.5 cm, diameter: 8.6 cm). Each window was irradiated by four tubular UV lamps (TL 4W/08 Black Light UVA lamps from Philips). Both sets of lamps were positioned parallel to the flat windows. The emission of the lamps ranged from 315 to 415 nm, with a maximum around 355 nm. In order to obtain diffuse radiation at the reactor windows, ground glass plates were placed between the lamps and reactor. The radiation flux entering the reactor, determined experimentally by ferrioxalate actinometry [50], was $6.3 \times 10^{-9} \text{ Einstein} \cdot \text{s}^{-1} \cdot \text{cm}^{-2}$ (2.15 mW cm^{-2}).

The reactor was part of a system operated in recirculation batch mode, as depicted in Figure 1. The set up consisted of a peristaltic pump, the reactor and a 1 L storage tank with a water jacket to maintain the temperature constant at 25 °C throughout the experiments. The tank contained a thermometer, a sample withdrawal system and a gas inlet to continuously bubble oxygen to keep the solution saturated with O₂.

Prior to experiments, a 1 L solution containing 20 mg·L⁻¹ of CA and the desired amount of the photocatalyst were mixed and sonicated for 30 minutes. Then, the suspension was added to the storage tank and recirculated in the system for 30 minutes with a pump flow rate of 1.5 L·min⁻¹ in order to allow the mixture to reach adsorption equilibrium. O₂ was bubbled into the storage tank and the lamps were switched on to stabilize emission. Shutters were placed between the lamps and the reactor to prevent any radiation from arriving to the suspension. Subsequently, the first sample was withdrawn from the tank (t=0), the shutters were removed, and the experiment started. Samples withdrawn from the tank at different irradiation times were centrifuged and filtered through a 0.02 µm syringe filters (Anotop 25) to remove photocatalyst particles before analysis. Photocatalytic experiments were carried out at pH 5 (natural pH) [35] under different catalysts concentrations: 25, 50, 100, and 250 mg L⁻¹.

2.6. Analysis

HPLC was used to quantify CA and the possible intermediates in a Waters chromatograph with a UV detector and a C-18 column. The mobile phase was a 70/30 mixture of acetonitrile/acidified water (with 0.1% v/v phosphoric acid). 20 µL of sample was injected with a flow rate of 1 mL·min⁻¹. Detection of CA and 4-CP was made at 227 nm whereas p-BQ was detected at 254 nm.

3. THEORETICAL MODELS

3.1. Estimation of the optical properties

In absorbing and scattering media, like photocatalysts suspensions, the distance travelled by a photon, the probability of being absorbed, and the directional distribution of the scattered radiation depend on the absorption coefficient (κ_λ), the scattering coefficient (σ_λ), and the phase function for scattering. It is important to note that optical properties depend on the wavelength of radiation, λ .

The extinction coefficient ($\beta_\lambda = \sigma_\lambda + \kappa_\lambda$) was estimated from extintance measurements of the photocatalysts suspensions as $\beta_\lambda = \frac{-\ln(T_\lambda)}{L}$, where T_λ is the normal transmittance at wavelength λ and L is the measuring cuvette path. In order to minimize the amount of scattered rays that reach the detector, a slit was placed before the detector according to the procedure previously reported [41]. Then, the specific extinction coefficient β_λ^* , per unit of catalyst mass concentration C_{cat} ($\beta_\lambda^* = \beta_\lambda / C_{cat}$), was obtained by applying linear regressions of the plots β_λ vs C_{cat} .

Diffuse reflectance and diffuse transmittance experimental measurements of the photocatalysts suspensions were carried out following the procedure described by Satuf et al. [42]. Simulation values of diffuse transmittance and reflectance were calculated by solving the RTE in the measuring cuvette employing the Monte Carlo method. The adjustable parameters of the model were the absorption coefficient (κ_λ) and the asymmetry factor (g_λ) included in the Henyey and Greenstein (HG) phase function. Finally, a nonlinear regression procedure was employed to adjust simulation values to experimental measurements [19, 40, 43, 51, 52].

The Monte Carlo method is a stochastic simulation procedure that, applied to radiation problems, consists on tracking the trajectory of the photons in a domain, in this case the measuring cuvette, with the aid of random numbers (R_i) between 0 and 1. The photocatalyst suspension inside the cuvette can be represented as a medium between two parallel infinite planes with azimuthal symmetry. Then, a one-dimensional, one-directional radiation transport model can be applied [41, 42], i.e. the flight path of the photons can be traced with one spatial variable (x) and one angular variable (θ). To describe the system, 1000 elementary volumes were considered in the simulations, in which photons could be either absorbed or scattered.

The main events considered in the Monte Carlo method to compute theoretical diffuse reflectance and transmittance values are detailed below and a scheme of the corresponding algorithm is shown in Figure 2. In addition, a schematic representation of the radiation field inside the cuvette can be found in Figures S1(A) and (B) of Supporting Information. The number of photons in the forward direction at $x=0$, $n_\lambda^+(x=0)$, selected in the simulation was 10^7 :

- 1) The direction of the photon that arrives at the inner wall of the cuvette ($x=0$) is assumed to be $\theta_0 = 0$ (collimated incident radiation)
- 2) Then, the length travelled by the photon in the catalyst suspension is calculated using the spectral extinction coefficient (β_λ):

$$l = -\frac{1}{\beta_\lambda} \ln(1 - R_1) \quad (1)$$

And the new position is computed as:

$$x_{new} = x_{old} + e_x l \quad (2)$$

where x_{old} represents the previous position and e_x is the direction cosine.

- 3) If the photon remains inside the quartz cuvette after travelling a distance l , the photon is considered to interact with a photocatalyst particle. The probability of absorption can be estimated with the albedo $\omega_\lambda = \sigma_\lambda / \beta_\lambda$. If

$$1 - \omega_\lambda \geq R_2 \quad (3)$$

the photon is absorbed, its trajectory ends and a new photon is generated. Otherwise, the photon is scattered and the new direction of the trajectory is calculated using the phase function. The Henyey and Greenstein (HG) phase function was adopted in this study since it provides suitable predictions of the photon trajectory in TiO_2 suspensions [42, 43, 53].

$$p_{HG,\lambda}(\cos\theta) = \frac{(1 - g_\lambda^2)}{2(1 + g_\lambda^2 - 2g_\lambda \cos\theta)^{\frac{3}{2}}} \quad (4)$$

where g_λ is the asymmetry factor. Thus, the angle θ that determines the new direction of the photon is given by:

$$\cos\theta = \frac{1}{2g_\lambda} \left[1 + g_\lambda^2 - \left(\frac{1 - g_\lambda^2}{1 + g_\lambda(2R_3 - 1)} \right)^2 \right] \quad (5)$$

Once the new direction is estimated, steps (2) and (3) are repeated until the photon is absorbed or it leaves the system through the cuvette walls.

- 4) If the new position of the photon is lower than 0 ($x < 0$), the photon is considered to leave the measuring cuvette through the irradiated wall, and it is counted as part of the reflected photons, $n_\lambda^-(x = 0)$. On the other hand, if the new position of the photon is higher than the cell length ($x > L$), the photon is stored inside the group of photons in the forward direction at the back wall of the cell, $n_\lambda^+(x = L)$.

- 5) $n_{\lambda}^{-}(x = 0)$ denotes the number of photons in the backward direction at the inner side of the front cuvette wall ($x=0$). To obtain the actual number of photons that leave the quartz cuvette at $x=-W$ and reach the detector, the effect of the wall is accounted as

$$n_{\lambda}^{-}(x = -W) = n_{\lambda}^{+}(x = -W)\Gamma_{\lambda} + n_{\lambda}^{-}(x = 0)Y_{\lambda} \quad (6)$$

where Y_{λ} and Γ_{λ} represent the global wall transmission coefficient and the global wall reflection coefficient, respectively [42].

- 6) $n_{\lambda}^{+}(x = L)$ represents the number of photons in the forward direction at the inner side of the back cuvette wall ($x=L$). To obtain the actual number of photons in the forward direction that leave the quartz cuvette at $x=L+W$ and reach the detector, the effect of the wall is accounted as

$$n_{\lambda}^{+}(x = L + W) = n_{\lambda}^{+}(x = L)Y_{\lambda} \quad (7)$$

Additionally, the incident photons that arrive at the inner side of the cuvette at $x=0$ ($n_{\lambda}^{+}(x = 0)$) are calculated as

$$n_{\lambda}^{+}(x = 0) = n_{\lambda}^{+}(x = -W)Y_{\lambda} \quad (8)$$

Then, the theoretical value of diffuse reflectance and diffuse transmittance were calculated according to the following expressions:

$$R_{\lambda} = \frac{n_{\lambda}^{-}(x = -W)}{n_{\lambda}^{+}(x = -W)} \quad (9)$$

$$T_{\lambda} = \frac{n_{\lambda}^{+}(x = L + W)}{n_{\lambda}^{+}(x = -W)} \quad (10)$$

A mathematical algorithm based on a nonlinear, multiparameter regression procedure was applied to obtain the values of the absorption coefficient (κ_{λ}) and the asymmetry factor (g_{λ}) that minimize the difference between predictions and experimental data. The spectral scattering coefficient was determined by:

$$\sigma_{\lambda} = \beta_{\lambda} - \kappa_{\lambda} \quad (11)$$

Finally, the specific absorption ($\kappa_{\lambda}^{*} = \kappa_{\lambda}/C_{Cat}$) and specific scattering ($\sigma_{\lambda}^{*} = \sigma_{\lambda}/C_{Cat}$) coefficients were obtained from the slopes of linear regressions between the κ_{λ} and σ_{λ} data versus C_{Cat} . The asymmetry factor was calculated as the average of the different g_{λ} values obtained for the different photocatalyst concentrations.

3.2. Calculation of the quantum efficiency

Numerous studies agree that the most suitable parameter to compare the intrinsic activity of a photocatalyst is the quantum efficiency (η) when polychromatic radiation is used [18, 54]. This parameter can be defined as the ratio of the observed initial molar reaction rate, $\langle r_{CA}(x, t_0) \rangle_{V_R}$, to the volumetric rate of photon absorption (VRPA) by the photocatalyst, $\langle e^a(x) \rangle_{V_R}$, both averaged over the reactor volume.

$$\eta = \frac{\langle r_{CA}(x, t_0) \rangle_{V_R}}{\langle e^a(x) \rangle_{V_R}} \quad (12)$$

η describes the efficiency of the absorbed photons to contribute to the chemical reaction.

3.2.1 Volumetric rate of photon absorption (VRPA)

The VRPA in the photoreactor was calculated by solving a radiation model with Monte Carlo simulations, employing the previously estimated optical parameters of the photocatalysts. In the reactor, the incoming radiation is diffuse (there is no preferential direction) because of the ground glass plates, and the photocatalysts suspensions produce the extinction of radiation mainly along the axial coordinate. Thus, the propagation of the radiation can be modelled with one spatial variable (x) and one angular variable (θ). The range of emission of the lamps was discretized in 11 wavelengths, every 10 nm from 315 to 415 nm, and the length of the reactor ($L_R=2.5$ cm) was divided into 1000 spatial cells ($\Delta x=0.0025$ cm). In these simulations, 10^7 photons of each wavelength were generated and traced until they left the reactor or were absorbed, in which case their position was stored. The main events considered in the Monte Carlo simulation are:

- 1) The incoming radiation was diffuse and, therefore, photons at the inner side of the reactor window had the same probability to follow any direction [53]. The angle θ that determines the direction of the photon was given by:

$$\sin \theta = 2R_1 - 1 \quad (13)$$

Steps 2) and 3) are the same as those detailed in Section 3.1.

The number of absorbed photons in each spatial cell Δx was stored as $n_{abs,\lambda}(x)$.

Finally the LVRPA in each cell was calculated by:

$$e^a(x) = \sum_{\lambda=315nm}^{\lambda=415nm} \frac{q_{w,\lambda} n_{abs,\lambda}(x)}{n_{tot} \Delta x} \quad (14)$$

where $q_{w,\lambda}$ is the inlet radiation flux of wavelength λ , and n_{tot} is the total number of photons considered in the simulation.

Finally, the average volumetric rate of photon absorption (VRPA) in the cylindrical reactor was calculated according to the following expression:

$$\langle e^a(x) \rangle_{V_R} = \frac{1}{L_R} \int_{x=0}^{x=L_R} e^a(x) dx \quad (15)$$

3.2.2 Reaction Rate

To calculate the quantum efficiency, apart from the VRPA, the initial volumetric reaction rate must be determined. For this purpose, the mass balance of clofibric acid (CA) was considered assuming that: (1) conversion per pass in the photoreactor is differential, (2) the system is well-mixed, (3) chemical reactions occur at the solid-liquid interface, (4) photolysis is negligible, and (5) there are no mass transfer limitations. Therefore, the mass balance for CA results:

$$\varepsilon_L \frac{dC_{CA}(t)}{dt} \Big|_{Tk} = -\frac{V_R}{V_T} \langle r_{CA}(x, t) \rangle_{V_R} \quad (16)$$

where ε_L is the liquid hold-up ($\varepsilon_L \approx 1$), C_{CA} represents the molar concentration of clofibric acid, V_R is the reactor volume, V_T is the total volume of the system and Tk refers to the storage tank. Thus, the initial reaction rate of clofibric acid photo-oxidation can be derived from the plot of the CA concentration in the tank versus time as follows:

$$\langle r_{CA}(x, t_0) \rangle_{V_R} = -\varepsilon_L \frac{V_T}{V_R} \lim_{t \rightarrow 0} \frac{\Delta C_{CA}(t) \Big|_{Tk}}{\Delta t} \quad (17)$$

4. RESULTS AND DISCUSSION

4.1. Photocatalyst characterization

From XRD patterns, shown in Figure 3, bare TiO_2 have presented a mixture of anatase and rutile crystalline phases. The percentage of each crystalline phase and the crystallite sizes, determined by the Scherrer equation, are given in Table 1, where the main physico-chemical properties of the TiO_2 -rGO nanocomposites are also summarized. Bare TiO_2 is mainly constituted by anatase (80%) with rutile (20%), with average crystallite sizes close to 17 and 21 nm, respectively. The presence of rGO in the nanocomposite did not introduce significant changes in both crystalline structure and average sizes of anatase and rutile, highlighting a slight increase in rutile crystalline phase when the rGO content was increased. Nevertheless, very similar XRD patterns were always found in all these P25-rGO nanocomposites in comparison to bare TiO_2 .

Whereas the graphene oxide employed to prepare the nanocomposites presents a clear diffraction peak at $2\theta=11.1^\circ$, when GO was subjected to the hydrothermal treatment (rGO) a very broad peak at $2\theta \sim 25^\circ$ was observed joined to the disappearance of the peak at $2\theta=11.1^\circ$, which indicates the reduction of graphene oxide. Moreover, no typical diffraction peak of GO was detected in any of the TiO_2 -rGO nanocomposites, probably because of the partial reduction of GO during the hydrothermal process and the low amount of GO added [22, 55-57].

Raman spectra of the photocatalysts were measured to verify the coexistence of rGO and TiO₂. Figure 4 shows the Raman spectra of GO, rGO, P25-rGO 0%, P25-rGO 0.1%, P25-rGO 0.5% and P25-rGO 1%, respectively. Bare TiO₂ and all P25-rGO nanocomposites have exhibited 5 distinct peaks at 143, 197, 399, 513 and 641 cm⁻¹, characteristic of the anatase crystalline phase [56, 58]; whereas a small peak, detected at 446 cm⁻¹, was ascribed to rutile [58]. Regarding GO, rGO and P25-rGO nanocomposites, Raman spectra of the characteristic peaks of graphitized carbon species at 1344 and 1602 cm⁻¹, attributed to the D band and the G band respectively, were also observed. In Table 1 the ratio of the area of the D band to the G band is also reported (A_D/A_G), which indicates the relative amount of defects compared to the sp² hybridized graphene domains [25, 56, 57]. GO and rGO yielded an A_D/A_G value close to 1.1, indicating a disordered structure even after GO was reduced by the hydrothermal treatment [24, 59], whereas values around 1.33 were estimated for the P25-rGO nanocomposites. The increase of the ratio is the result of the strong interaction between TiO₂ and rGO sheets after the hydrothermal method, plus the contribution of remaining surface oxygenated functional groups [24, 56, 60, 61].

Morphology of the synthesized photocatalysts was studied by SEM and TEM and the corresponding images are shown in Figures 5 and 6, respectively.

SEM images of P25-rGO 0% and P25-rGO 1% can be seen in Figures 5a and 5b, respectively. These photocatalysts, regardless the presence of rGO, are constituted by small spherical TiO₂ nanoparticles with similar sizes, ranging from 20 to 40 nm. These primary particles led to the formation of densely packed agglomerates. Although isolated rGO sheets were hard to find probably because of the low amount of GO added to the TiO₂-rGO nanocomposite, exposed rGO surface without TiO₂ nanoparticles should be easier to spot on increasing the rGO/TiO₂ ratio [55].

Finally, in Figure 5c is shown the EDX pattern of P25-rGO 1% photocatalyst. A peak ascribed to C was observed in the EDX spectrum which further evidences the presence of rGO in the nanocomposites.

In order to understand the morphology and microstructure of these photocatalysts TEM studies were also carried out. Figure 6a shows a TEM micrograph of bare TiO₂, consisting in particles of TiO₂ of around 20-40 nm size that form aggregates. The obtained results in XRD patterns, from which it was concluded that bare TiO₂ and the corresponding TiO₂-rGO photocatalysts were constituted by a mixture of mainly anatase with rutile crystalline phases, were in accordance with the results obtained from TEM and electron diffraction studies where the predominant crystalline phase was always anatase. An HRTEM image of one of these anatase particles down the [131] zone axis is presented in Figure 6b.

When rGO was present some features can be highlighted; a representative image of one aggregate can be observed in Figure 6c. Different regions of this aggregate were analyzed in

detail, marked with squares in Figure 6c, and their corresponding HRTEM images are shown in the Figures 6d, 6e and 6f. Attending to Figure 6d, the rGO sheet can be seen isolated at the edge of the particles (red arrow), but also crumpled over them (blue arrows). This later fact could be observed almost over the entire aggregate, as it is also noticeable in Fig. 6e. Here, it could also be appreciated that some particles seem to be wrapped with few layers of the rGO (green arrow). This intimate contact of the particles with the rGO sheets is more clearly observed in Fig. 6f, where some particles were at least partially if not completely surrounded by the rGO sheet. These observations evinced the good contact between the TiO₂ particles and the rGO.

UV-visible absorption properties of these photocatalysts powders were analyzed by measuring the UV-vis diffuse reflectance spectra (DRS). Band gap energy (E_g) was estimated through the Tauc plot and the corresponding values are shown in Table 1 [46]. E_g values of 3.1 ± 0.1 were obtained for all the photocatalysts, indicating that the presence of rGO did not entail the formation of new energy levels in the band gap.

Considering the BET surface area, no differences were observed among bare TiO₂ and the TiO₂-rGO composites, with surface area values around $57 \text{ m}^2 \cdot \text{g}^{-1}$ (see Table 1).

4.2. Optical properties of the photocatalyst suspensions

The plots of the specific scattering and absorption coefficients and the asymmetry factor as a function of the wavelength for P25-rGO 0%, P25-rGO 0.1%, P25-rGO 0.5% and P25-rGO 1% suspensions are shown in Figures 7 and the values corresponding to P25-rGO 0.5% can be found in Table S1 of the Supporting Information.

Regarding absorption coefficients, a notable increase is observed at short wavelengths, below 325 nm, when the GO:TiO₂ mass ratio increases up to 0.5%. In contrast, P25-rGO 1% photocatalyst exhibits slightly lower values of the absorption coefficient when is compared to P25-rGO 0%.

As to scattering coefficient, the higher the amount of rGO present in the nanocomposite, the higher the scattering coefficient values. In fact, rGO seems to have greater effect on radiation scattering than on absorption.

It can also be noticed that below 335 nm (see Figure 7), the values of the absorption coefficient exceeds those of the scattering coefficient. However, above that wavelength, opposite behaviour was found, with absorption coefficient values being nearly five times lower than the scattering coefficient.

A rise in the value of the asymmetry factor was observed when rGO was added to the TiO₂. The asymmetry factor ranged between 0.4-0.63 for P25-rGO 0% and 0.55-0.68 for P25-rGO 1%. This positive value indicates that light scattered by the TiO₂-rGO suspensions occurred mainly in the forward direction and the addition of rGO favours the scattering in that direction.

4.3. Photocatalytic activity

The temporal evolution of clofibric acid concentration and its main reaction intermediates, 4-chlorophenol (4-CP) and p-benzoquinone (p-BQ), using different loadings of P25-rGO 0%, 0.1% 0.5% and 1% can be found in Figures 8 and Figures S2-S5 of the Supporting Information. In all photodegradation runs the concentration evolution of the organic compounds was always very similar. 4-CP concentration was always higher than p-BQ concentration, and 4-CP concentration exceeded CA concentration after 4-5 h of photodegradation. Concerning the concentration evolution observed when P25-rGO 0.5% was used (Figures 8 and Figures S4), negligible concentrations of CA and intermediates remained in the reaction medium after 6 h of irradiation time when catalyst loadings of 50 mg·L⁻¹ or higher were used.

Under our experimental conditions, degradation of CA followed pseudo-first order kinetics. The effect of the photocatalyst concentration on the apparent reaction rate constant k for the different nanocomposites is presented in Table 2. The apparent kinetic constant always increased when increasing the catalyst concentration up to 100 mg L⁻¹. Regarding the amount of rGO, the value of k increased when increasing the rGO content, reaching a maximum value with P25-rGO 0.5%, and then decreased for P25-rGO 1%.

The performance of the catalysts presented the following order: P25-rGO 0.5% > P25-rGO 0.1% \approx P25-rGO 0% > P25-rGO 1%. It could be noted that the addition of rGO to TiO₂ led to a slight increase in the apparent reaction rate constant values. This improvement in clofibric acid photodegradation can be ascribed to the role played by rGO, since it is able to lower the charge transfer resistance and act as an electron acceptor, which helps to decrease the recombination rate of electron-hole pairs [31, 62-65]. As a consequence, a higher amount of charge carriers can enable to generate reactive species such as holes or hydroxyl radicals [28]. However, an excess on the rGO loading can lead to a reduction of the photocatalytic activity ascribed to two reasons: (1) a shielding effect caused by rGO that blocks light and prevents radiation from being absorbed by TiO₂, and (2) when the amount of rGO is excessive, it could act as recombination center [31, 61, 66-68]. Because the highest photocatalytic activity was obtained with P25-rGO 0.5%, this nanocomposite was selected for further comparison with bare TiO₂. It should be mentioned that experiments with catalyst concentrations of 250 mg L⁻¹ were also carried out, but no significant improvements in the photoreaction rates were observed when they were compared with 100 mg L⁻¹.

Table 3 presents the values of initial reaction rate, VRPA, and quantum efficiency for P25-rGO 0% and P25-rGO 0.5% photocatalysts. Similar values of VRPA were obtained with bare and nanocomposite catalysts, both increasing with the catalyst concentration. Regarding the quantum efficiency, the highest value was achieved with P25-rGO 0.5% at 100 mg L⁻¹ whose

quantum efficiency value was 11% higher than that obtained with P25-rGO 0%. Since the absorbed radiation estimated for both photocatalysts was nearly the same, it could be concluded that the improvement in the performance of the photocatalytic activity of P25-rGO 0.5% was due to a reduction of the charge carriers recombination rate [24-26, 69, 70].

5. CONCLUSIONS

In this work, TiO₂-rGO nanocomposites were hydrothermally prepared and compared through their physico-chemical properties and photoactivity in the degradation of clofibric acid. Raman spectra indicated a strong interaction between TiO₂ and rGO layers, further confirmed by TEM images.

The optical properties of TiO₂-rGO nanocomposites were estimated from UV-visible measurements in the range 315-415 nm. The presence of rGO increased the scattering coefficient in the whole UV-A range, whereas the effect on the absorption coefficient was notable only at wavelengths lower than 325 nm. P25-rGO 0.5% exhibited the highest absorption coefficients and P25-rGO 1%, the lowest. The asymmetry factor (around 0.55) for all photocatalysts indicated that radiation is preferentially scattered in the forward direction.

Radiation absorption inside the photocatalytic reactor was computed by using the Monte Carlo method. Complete degradation of clofibric acid was achieved after 6 h of irradiation time and the maximum initial reaction rates were obtained when 100 mg·L⁻¹ of the photocatalysts were used. P25-rGO 0.5% and P25-rGO 1% led to the highest and lowest photocatalytic activities, respectively. The lowest photodegradation found in P25-rGO 1% was ascribed to an excess of rGO that could favor charge carriers recombination leading to detrimental photoactivity. The highest value of quantum efficiency was achieved with P25-rGO 0.5% at 100 mg L⁻¹, with an increase of 11% compared to the value obtained for P25-rGO 0%.

Acknowledgements

This work has been supported by the Spanish Plan Nacional de I+D+i through the project CTM2015-64895-R and CTM2016-76454-R. Alvaro Tolosana-Moranchel thanks Ministerio de Educación, Cultura y Deporte for his FPU grant (FPU14/01605) and (EST17/00110). The authors are also grateful to Universidad Nacional del Litoral (UNL), Consejo Nacional de Investigaciones Científicas y Técnicas (CONICET), and Agencia Nacional de Promoción Científica y Tecnológica (ANPCyT) for financial support. We also thank Antonio C. Negro for his valuable help during the experimental work.

NOMENCLATURE

C_{cat} = mass catalyst concentration, $\text{g}\cdot\text{L}^{-1}$

C_i = molar concentration of compound i in the bulk, $\text{mmol}\cdot\text{L}^{-1}$

CA = clofibric acid

$e^a(x)$ = local volumetric rate of photon absorption, $\text{Einstein}\cdot\text{cm}^{-3}\cdot\text{s}^{-1}$

E_g = band gap energy, eV

4-CP = 4-chlorophenol

g = asymmetry factor, dimensionless

k = apparent kinetic constant, h^{-1}

LVRPA = local volumetric rate of photon absorption, $\text{Einstein}\cdot\text{cm}^{-3}\cdot\text{s}^{-1}$

p = phase function, dimensionless

p-BQ = p-benzoquinone

q = radiation flux, $\text{Einstein}\cdot\text{cm}^{-2}\cdot\text{s}^{-1}$

R = value of a reflectance spectrophotometric measurement

$(-r_i)$ = photodegradation rate of compound i, $\text{mol}\cdot\text{cm}^{-3}\cdot\text{s}^{-1}$

S_{BET} = catalyst specific surface area, $\text{m}^2\cdot\text{g}^{-1}$

T = value of a transmittance spectrophotometric measurement

t = time

V = Volume

VRPA = volumetric rate of photon absorption, $\text{Einstein}\cdot\text{cm}^{-3}\cdot\text{s}^{-1}$

Y = global transmission coefficient of the reactor windows

W = wall thickness, cm

Greek letters

α = absorption coefficient of the semiconductor, cm^{-1}

β = extinction coefficient, cm^{-1}

η = quantum efficiency, $\text{mol}\cdot\text{Einstein}^{-1}$

κ =absorption coefficient, cm^{-1}

λ = wavelength, nm

Γ =global reflection coefficient of the reactor windows

θ = spherical coordinate, rad

σ = scattering coefficient, cm^{-1}

ω = spectral albedo

Subscripts

4-CP = relative to 4-chlorophenol

0 = initial value or relative to the reactor window at $x=0$

λ = indicates a dependence on wavelength

CA = relative to clofibric acid

Cat = relative to catalyst

L= relative to the reactor window at $x = L$

p-BQ = relative to p-benzoquinone

R=reactor

T = total

Tk= tank

V_R = relative to reactor volume

W=wall

Superscripts

* = specific properties

+ = forward direction

– = backward direction

Special symbols

$\langle \rangle$ = average value over a defined space

6. REFERENCES

- [1] N.H. Tran, M. Reinhard, K.Y.H. Gin, *Water Research* 133 (2018) 182-207.
- [2] N. Serpone, Y.M. Artemev, V.K. Ryabchuk, A.V. Emeline, S. Horikoshi, *Current Opinion in Green and Sustainable Chemistry* 6 (2017) 18-33.
- [3] B.H. Schafhauser, L.A. Kristofco, C.M.R. de Oliveira, B.W. Brooks, *Environmental Pollution* 238 (2018) 440-451.
- [4] S. Sakalli, P.T. Giang, V. Burkina, G. Zamaratskaia, M.K. Rasmussen, T. Bakal, S.K. Tilami, S. Sampels, J. Kolarova, R. Grabic, J. Turek, T. Randak, V. Zlabek, *Science of the Total Environment* 635 (2018) 1160-1169.
- [5] Y. He, S. Nurul, H. Schmitt, N.B. Sutton, T.A.J. Murk, M.H. Blokland, H.H.M. Rijnaarts, A.A.M. Langenhoff, *Science of the Total Environment* 631-632 (2018) 1572-1581.
- [6] E. Szabados, A. Jobbágy, A.J. Tóth, P. Mizsey, G. Tardy, C. Pulgarin, S. Giannakis, E. Takács, L. Wojnárovits, M. Makó, Z. Trócsányi, A. Tungler, *Periodica Polytechnica Chemical Engineering* 62 (2018) 76-90.
- [7] A.A. Renita, P.S. Kumar, S. Srinivas, S. Priyadharshini, M. Karthika, *Desalination and Water Treatment* 87 (2017) 160-178.
- [8] S. Álvarez-Torrellas, M. Munoz, J. Gläsel, Z.M. de Pedro, C.M. Domínguez, J. García, B.J.M. Etzold, J.A. Casas, *Chemical Engineering Journal* 347 (2018) 595-606.
- [9] L. Sbardella, J. Comas, A. Fenu, I. Rodriguez-Roda, M. Weemaes, *Science of The Total Environment* 636 (2018) 519-529.
- [10] S. Malato, P. Fernández-Ibáñez, M.I. Maldonado, J. Blanco, W. Gernjak, *Catalysis Today* 147 (2009) 1-59.
- [11] J. Schneider, M. Matsuoka, M. Takeuchi, J. Zhang, Y. Horiuchi, M. Anpo, D.W. Bahnemann, *Chemical Reviews* 114 (2014) 9919-9986.
- [12] A. Hakki, J. Schneider, D. Bahnemann, *Photocatalysis: Fundamentals and Perspectives*, The Royal Society of Chemistry, 2016, pp. 29-50.
- [13] P. Calza, C. Hadjicostas, V.A. Sakkas, M. Sarro, C. Minero, C. Medana, T.A. Albanis, *Applied Catalysis B: Environmental* 183 (2016) 96-106.
- [14] T.E. Doll, F.H. Frimmel, *Water Research* 38 (2004) 955-964.
- [15] J. Ye, *Photocatalysis: Fundamentals and Perspectives*, The Royal Society of Chemistry, 2016, pp. 245-251.
- [16] T. Szabó, Á. Veres, E. Cho, J. Khim, N. Varga, I. Dékány, *Colloids and Surfaces A: Physicochemical and Engineering Aspects* 433 (2013) 230-239.
- [17] F. Machuca-Martinez, M.A. Mueses, J. Colina-Marquez, G.L. Puma, *Photocatalysis: Fundamentals and Perspectives*, The Royal Society of Chemistry, 2016, pp. 388-424.
- [18] J. Marugan, R. van Grieken, A.E. Cassano, O.M. Alfano, *Photocatalysis: Fundamentals and Perspectives*, The Royal Society of Chemistry, 2016, pp. 367-387.
- [19] P.J. Valadés-Pelayo, F. Guayaquil Sosa, B. Serrano, H. de Lasa, *Chemical Engineering Science* 126 (2015) 42-54.
- [20] Y. Wu, M. Wark, *Photocatalysis: Fundamentals and Perspectives*, The Royal Society of Chemistry, 2016, pp. 129-161.
- [21] L.L. Tan, S.P. Chai, A.R. Mohamed, *ChemSusChem* 5 (2012) 1868-1882.
- [22] W. Fan, Q. Lai, Q. Zhang, Y. Wang, *The Journal of Physical Chemistry C* 115 (2011) 10694-10701.
- [23] G.S. Anjusree, A.S. Nair, S.V. Nair, S. Vadukumpully, *RSC Advances* 3 (2013) 12933.

- [24] P. Ribao, M.J. Rivero, I. Ortiz, *Environmental Science and Pollution Research* 24 (2017) 12628-12637.
- [25] P. Fernández-Ibáñez, M.I. Polo-López, S. Malato, S. Wadhwa, J.W.J. Hamilton, P.S.M. Dunlop, R. D'Sa, E. Magee, K. O'Shea, D.D. Dionysiou, J.A. Byrne, *Chemical Engineering Journal* 261 (2015) 36-44.
- [26] H. Adamu, P. Dubey, J.A. Anderson, *Chemical Engineering Journal* 284 (2016) 380-388.
- [27] M. Faraldos, A. Bahamonde, *Catalysis Today* 285 (2017) 13-28.
- [28] K. Alamelu, V. Raja, L. Shiamala, B.M. Jaffar Ali, *Applied Surface Science* 430 (2018) 145-154.
- [29] M. Wu, L. Gu, Q. Wang, C. Wang, H. Zhang, *ChemNanoMat* 4 (2018) 387-393.
- [30] Z. Zhu, F. Zhou, S. Zhan, Y. Tian, Q. He, *Applied Surface Science* 430 (2018) 116-124.
- [31] W. Wang, J. Yu, Q. Xiang, B. Cheng, *Applied Catalysis B: Environmental* 119-120 (2012) 109-116.
- [32] D. Xu, B. Cheng, W. Wang, C. Jiang, J. Yu, *Applied Catalysis B: Environmental* 231 (2018) 368-380.
- [33] M.A. Mueses, F. Machuca-Martinez, G. Li Puma, *Chemical Engineering Journal* 215-216 (2013) 937-947.
- [34] M.A. Mueses, F. Machuca-Martinez, A. Hernández-Ramírez, G. Li Puma, *Chemical Engineering Journal* 279 (2015) 442-451.
- [35] A. Manassero, M.L. Satuf, O.M. Alfano, *Environmental Science and Pollution Research* 22 (2015) 926-937.
- [36] J. Marugán, R. van Grieken, C. Pablos, M.L. Satuf, A.E. Cassano, O.M. Alfano, *Catalysis Today* 240 (2015) 9-15.
- [37] J. Marugán, R. Van Grieken, A.E. Cassano, O.M. Alfano, *Photocatalytic reactor design*, RSC Energy and Environment Series, 2016, pp. 367-387.
- [38] O.M. Alfano, A.E. Cassano, J. Marugan, R. van Grieken, *Photocatalysis: Fundamentals and Perspectives*, The Royal Society of Chemistry, 2016, pp. 349-366.
- [39] A. Manassero, M.L. Satuf, O.M. Alfano, *Environmental Science and Pollution Research* 24 (2017) 6031-6039.
- [40] P.J. Valadés-Pelayo, J. Moreira del Rio, P. Solano-Flores, B. Serrano, H. de Lasa, *Chemical Engineering Science* 116 (2014) 406-417.
- [41] M.I. Cabrera, O.M. Alfano, A.E. Cassano, *The Journal of Physical Chemistry* 100 (1996) 20043-20050.
- [42] M.L. Satuf, R.J. Brandi, A.E. Cassano, O.M. Alfano, *Industrial & Engineering Chemistry Research* 44 (2005) 6643-6649.
- [43] P.J. Valades-Pelayo, J. Moreira, B. Serrano, H. de Lasa, *Chemical Engineering Science* 107 (2014) 123-136.
- [44] M.L. Satuf, R.J. Brandi, A.E. Cassano, O.M. Alfano, *Applied Catalysis B: Environmental* 82 (2008) 37-49.
- [45] T.E. Doll, F.H. Frimmel, *Water Research* 39 (2005) 403-411.
- [46] H.N.D. Zhebo Chen, Eric Miller, *Photoelectrochemical Water Splitting Standards, Experimental Methods, and Protocols*, Springer New York, 2013.
- [47] R.L.Z. R. Jenkins, *Introduction to X-Ray powder Diffractometry*, John Wiley & Sons Inc., New York, 1996.
- [48] R.A. Spurr, H. Myers, *Analytical Chemistry* 29 (1957) 760-762.
- [49] S. Brunauer, P.H. Emmett, E. Teller, *Journal of the American Chemical Society* 60 (1938) 309-319.
- [50] I.C. S.L. Murov, G.L. Hug, *Handbook of Photochemistry*, Second ed., Marcel Dekker, New York, 1993.
- [51] J. Moreira, B. Serrano, A. Ortiz, H. de Lasa, *Industrial & Engineering Chemistry Research* 49 (2010) 10524-10534.
- [52] J. Moreira, B. Serrano, A. Ortiz, H. de Lasa, *Chemical Engineering Science* 66 (2011) 5813-5821.

- [53] A. Manassero, M.L. Satuf, O.M. Alfano, *Environmental science and pollution research international* 22 (2015) 926-937.
- [54] A. Manassero, M.L. Satuf, O.M. Alfano, *Chemical Engineering Journal* 326 (2017) 29-36.
- [55] M. Cao, P. Wang, Y. Ao, C. Wang, J. Hou, J. Qian, *Chemical Engineering Journal* 264 (2015) 113-124.
- [56] T. Liu, B. Liu, L. Yang, X. Ma, H. Li, S. Yin, T. Sato, T. Sekino, Y. Wang, *Applied Catalysis B: Environmental* 204 (2017) 593-601.
- [57] K.-Q. Lu, Y. Chen, X. Xin, Y.-J. Xu, *Applied Catalysis B: Environmental* 224 (2018) 424-432.
- [58] D.A.H. Hanaor, C.C. Sorrell, *Journal of Materials Science* 46 (2011) 855-874.
- [59] A.W. Morawski, E. Kusiak-Nejman, A. Wanag, J. Kapica-Kozar, R.J. Wróbel, B. Ohtani, M. Aksienionek, L. Lipińska, *Catalysis Today* 280 (2017) 108-113.
- [60] S. Kaniyankandy, S.N. Achary, S. Rawalekar, H.N. Ghosh, *The Journal of Physical Chemistry C* 115 (2011) 19110-19116.
- [61] A. Morais, C. Longo, J.R. Araujo, M. Barroso, J.R. Durrant, A.F. Nogueira, *Physical Chemistry Chemical Physics* 18 (2016) 2608-2616.
- [62] A. Tolosana-Moranchel, J.A. Casas, A. Bahamonde, L. Pascual, L.I. Granone, J. Schneider, R. Dillert, D.W. Bahnemann, *Applied Catalysis B: Environmental* 241 (2019) 375-384.
- [63] W. Liu, Y. Gao, Y. Yang, Q. Zou, G. Yang, Z. Zhang, H. Li, Y. Miao, H. Li, Y. Huo, *ChemCatChem* 10 (2018) 2394-2400.
- [64] C. Han, N. Zhang, Y.-J. Xu, *Nano Today* 11 (2016) 351-372.
- [65] Y. Zhang, Z.-R. Tang, X. Fu, Y.-J. Xu, *ACS Nano* 5 (2011) 7426-7435.
- [66] M. Minella, F. Sordello, C. Minero, *Catalysis Today* 281 (2017) 29-37.
- [67] Y. Zhang, Z.-R. Tang, X. Fu, Y.-J. Xu, *ACS Nano* 4 (2010) 7303-7314.
- [68] K.-Q. Lu, X. Xin, N. Zhang, Z.-R. Tang, Y.-J. Xu, *Journal of Materials Chemistry A* 6 (2018) 4590-4604.
- [69] B.R. Cruz-Ortiz, J.W.J. Hamilton, C. Pablos, L. Díaz-Jiménez, D.A. Cortés-Hernández, P.K. Sharma, M. Castro-Alfárez, P. Fernández-Ibañez, P.S.M. Dunlop, J.A. Byrne, *Chemical Engineering Journal* 316 (2017) 179-186.
- [70] M. Faraldos, A. Bahamonde, *Catalysis Today* 285 (2017) 13-28.

Table 1. Physico-chemical properties of TiO₂ and TiO₂-rGO photocatalysts.

Photocatalyst	Anatase	Rutile	d _{Anatase}	d _{Rutile}	Band gap	A _D /A _G *	S _{BET}
	(%)	(%)	(nm)	(nm)	(eV)	a.u.	(m ² ·g ⁻¹)
P25-rGO 0%	80	20	16.7	21.1	3.1	-	53
P25-rGO 0.1%	78	22	18.4	26.4	3.1	1.37	54
P25-rGO 0.5%	76	24	18.4	25.5	3.1	1.33	56
P25-rGO 1%	76	24	16.3	20.5	3.1	1.33	58

* The ratio A_D/A_G was 1.13 and 1.14 for GO and rGO respectively

Table 2. Apparent kinetic constant k (h^{-1}) for TiO_2 and TiO_2 -rGO photocatalysts.

C_{Cat} ($\text{mg}\cdot\text{L}^{-1}$)	P25-rGO 0%	P25-rGO 0.1%	P25-rGO 0.5%	P25-rGO 1%
25	0.438	0.450	0.461	0.413
50	0.542	0.534	0.543	0.427
100	0.608	0.616	0.675	0.515
250	0.619	0.566	0.631	0.552

Table 3. Influence of photocatalyst concentration on initial rate of CA photodegradation, VRPA and quantum efficiency for P25-rGO 0% and P25-rGO 0.5%.

	$\langle -r_{CA}(x, t_0) \rangle_{V_R} (\text{mol s}^{-1} \cdot \text{cm}^{-3}) \times 10^{11}$		VRPA ($\text{Einstein} \cdot \text{s}^{-1} \cdot \text{cm}^{-3}$) $\times 10^9$		$\eta (\text{mol} \cdot \text{Einstein}^{-1}) \times 10^2$	
$C_{\text{Cat}} (\text{mg} \cdot \text{L}^{-1})$	P25-rGO 0%	P25-rGO 0.5%	P25-rGO 0%	P25-rGO 0.5%	P25-rGO 0%	P25-rGO 0.5%
25	7.81	8.22	4.51	4.62	1.73	1.78
50	9.66	9.68	4.91	4.94	1.97	1.96
100	10.84	12.03	4.97	4.96	2.18	2.42

Figure

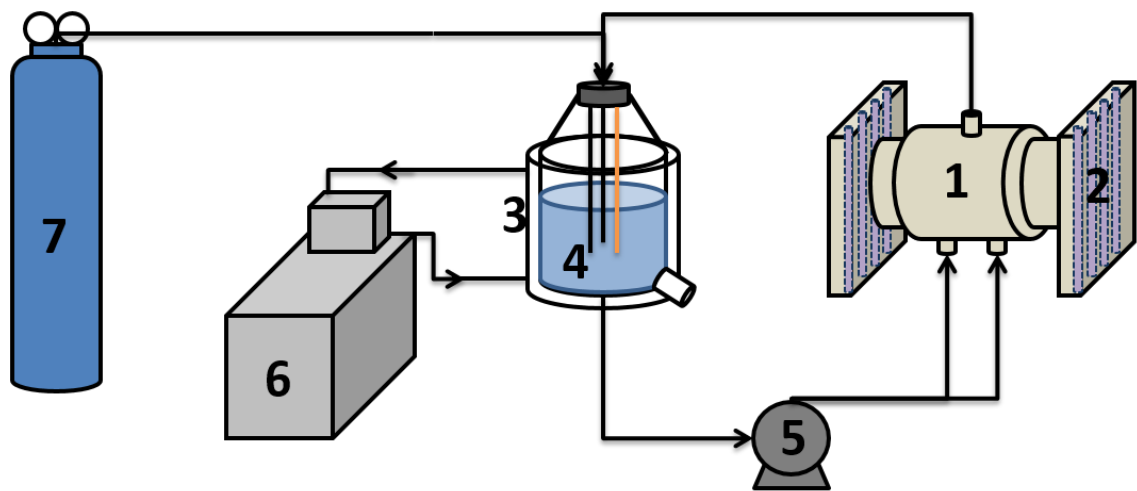


Figure 1. Photoactivity experimental set-up: (1), photoreactor; (2), UV lamps; (3), water jacket; (4), storage tank; (5), pump; (6), thermostatic bath; (7), oxygen.

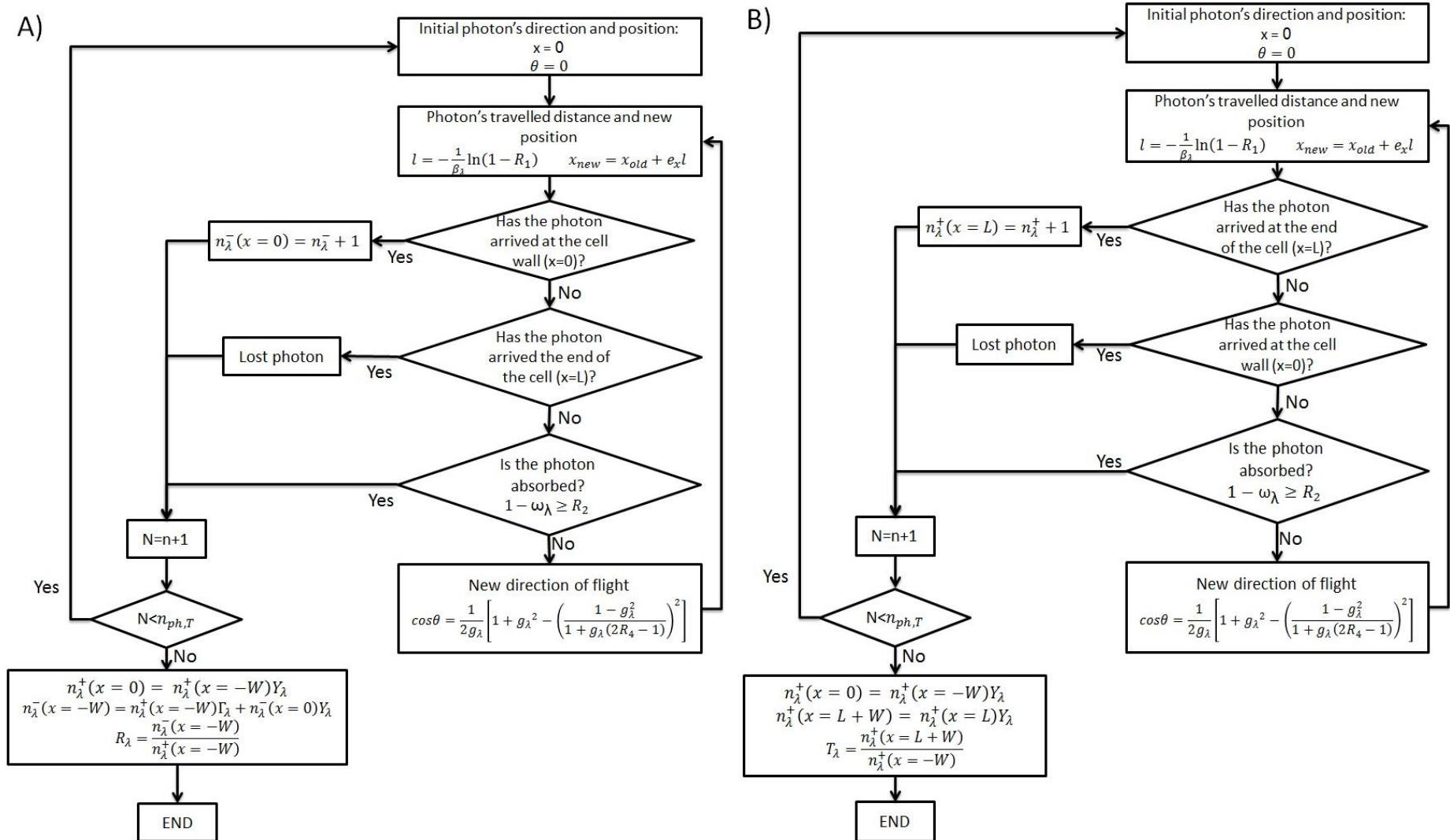


Figure 2. Scheme of the Monte Carlo method used to calculate the theoretical diffuse reflectance (A) and diffuse transmittance (B) value.

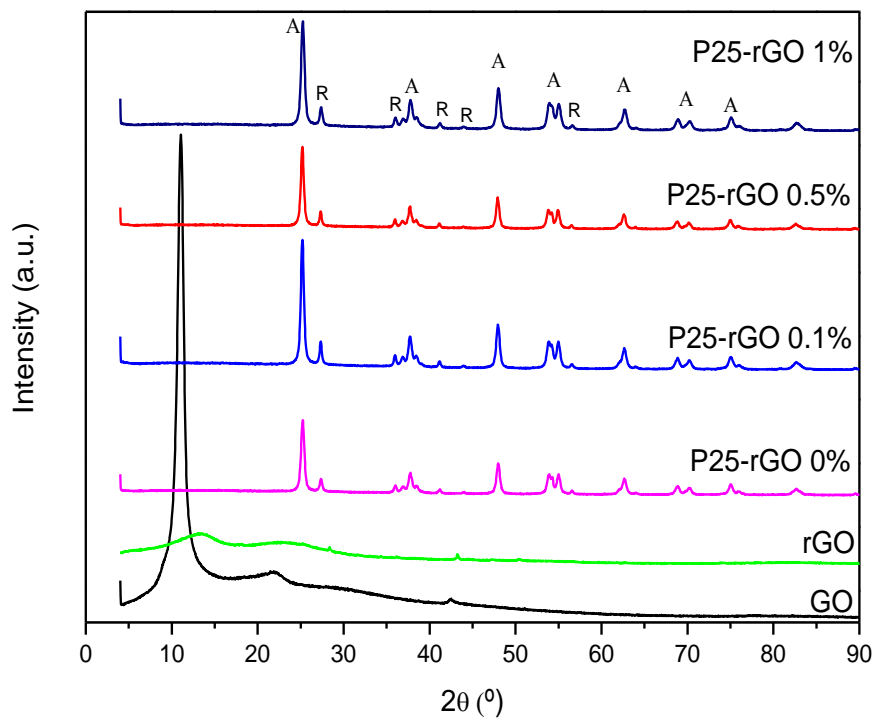
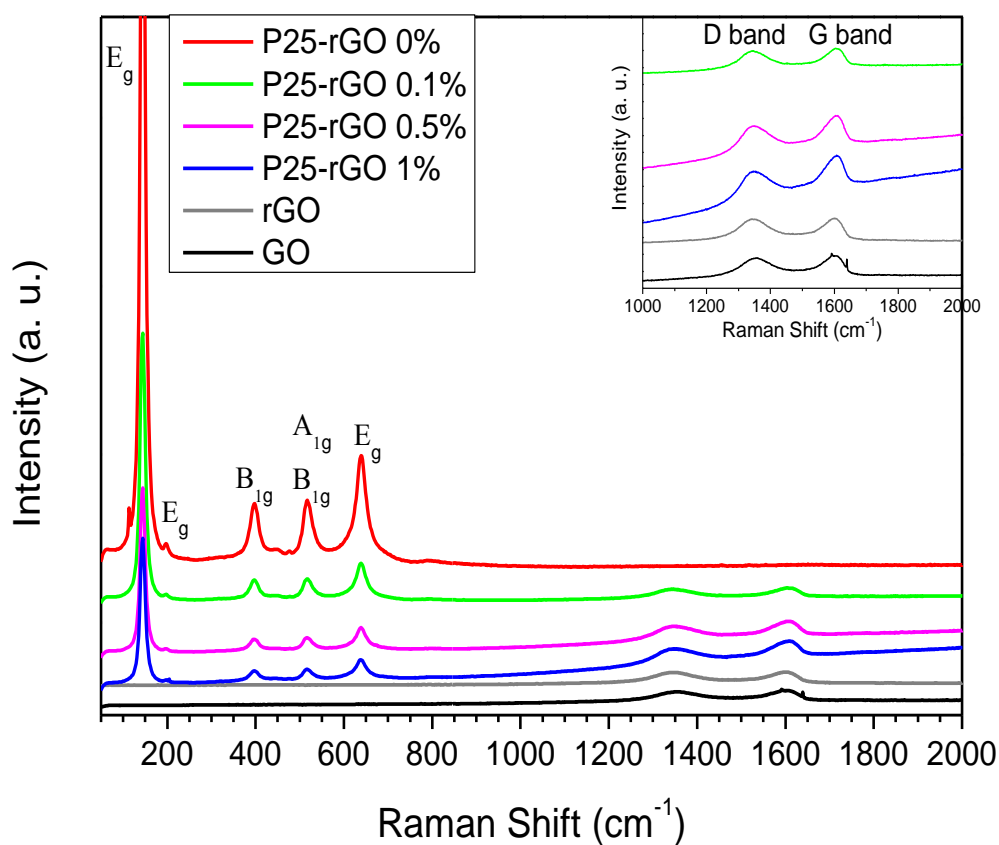
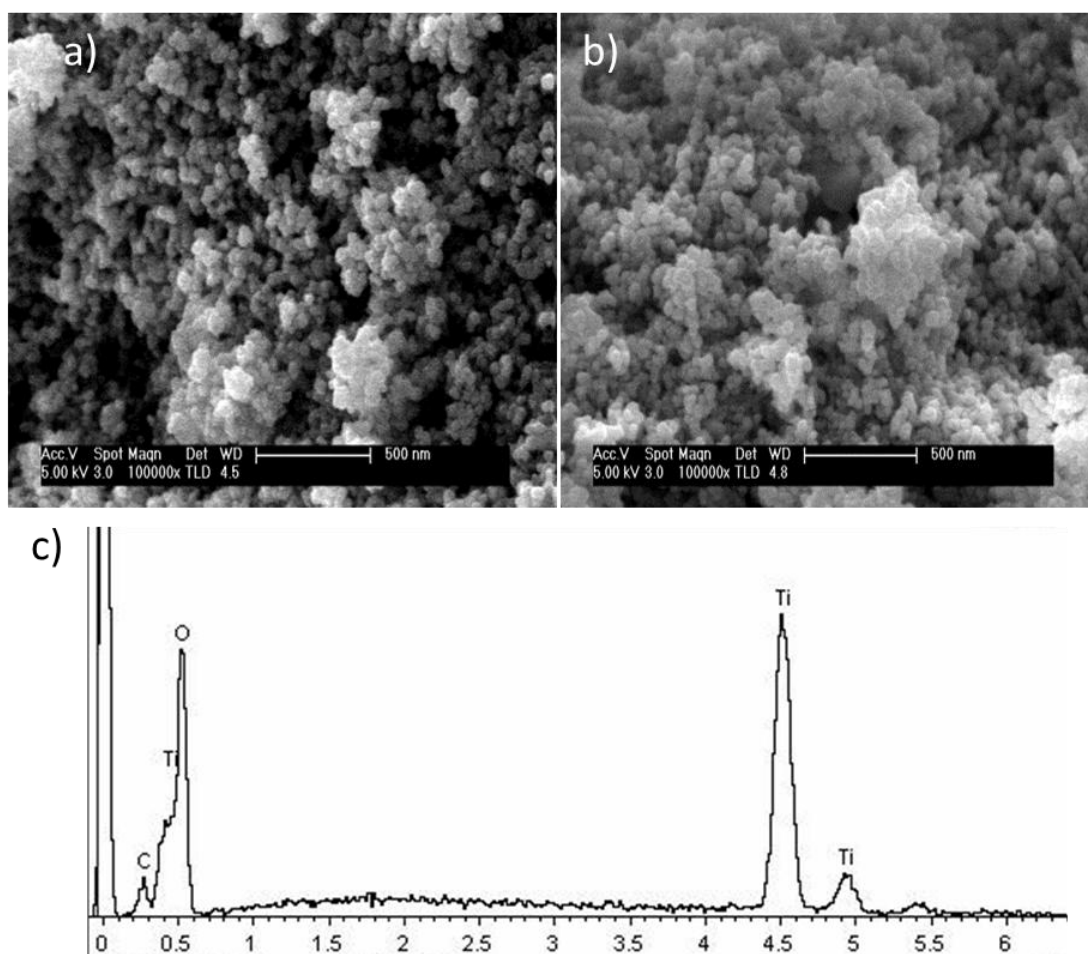


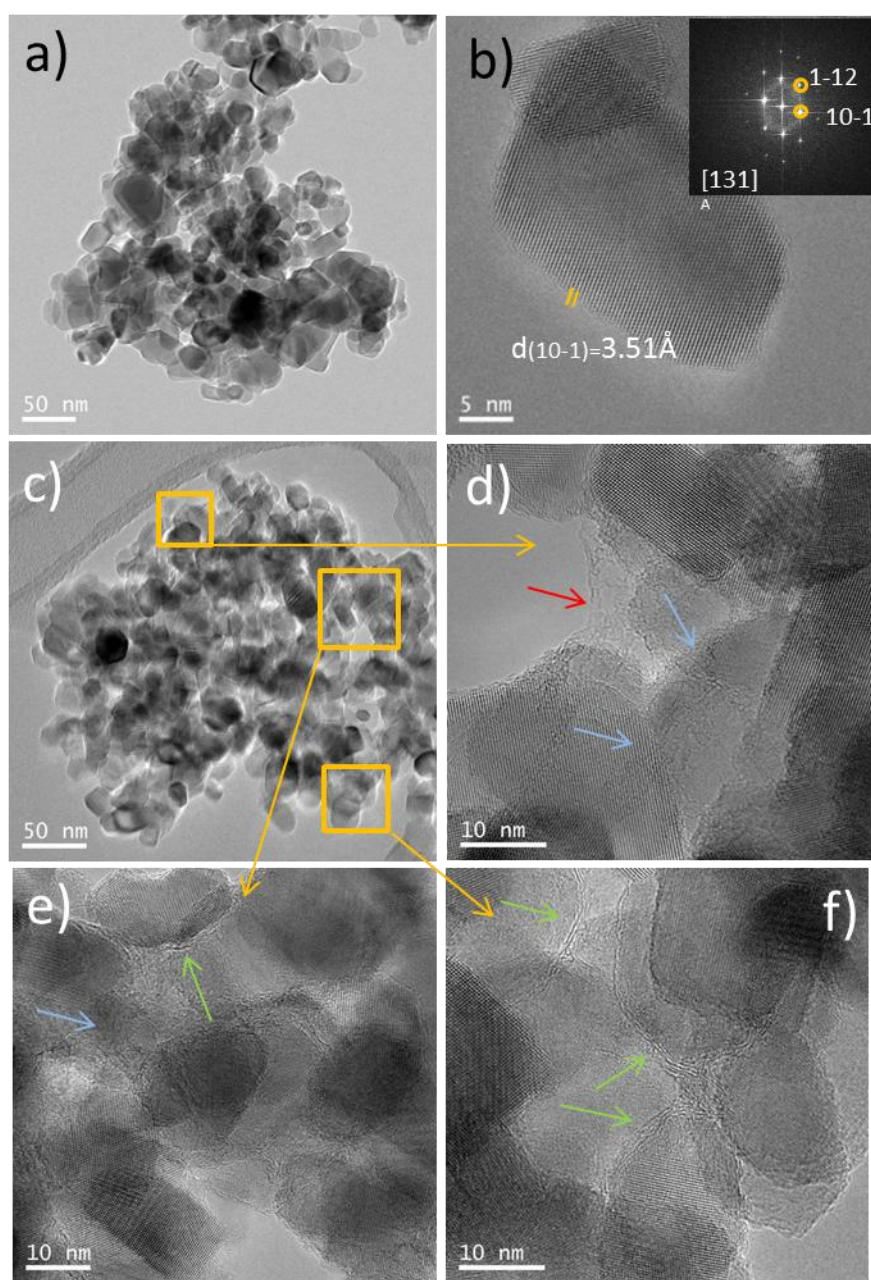
Figure 3. XRD patterns of pure GO, rGO, and P25-rGO 0%, P25-rGO 0.1%, P25-rGO 0.5% and P25-rGO 1% photocatalysts.



Figures 4. Raman spectra of GO, rGO and P25-rGO 0%, P25-rGO 0.1%, P25-rGO 0.5%, and P25-rGO 1% photocatalyst. (upper right) Raman magnified spectra ranging from 1000 cm^{-1} to 2000 cm^{-1} .

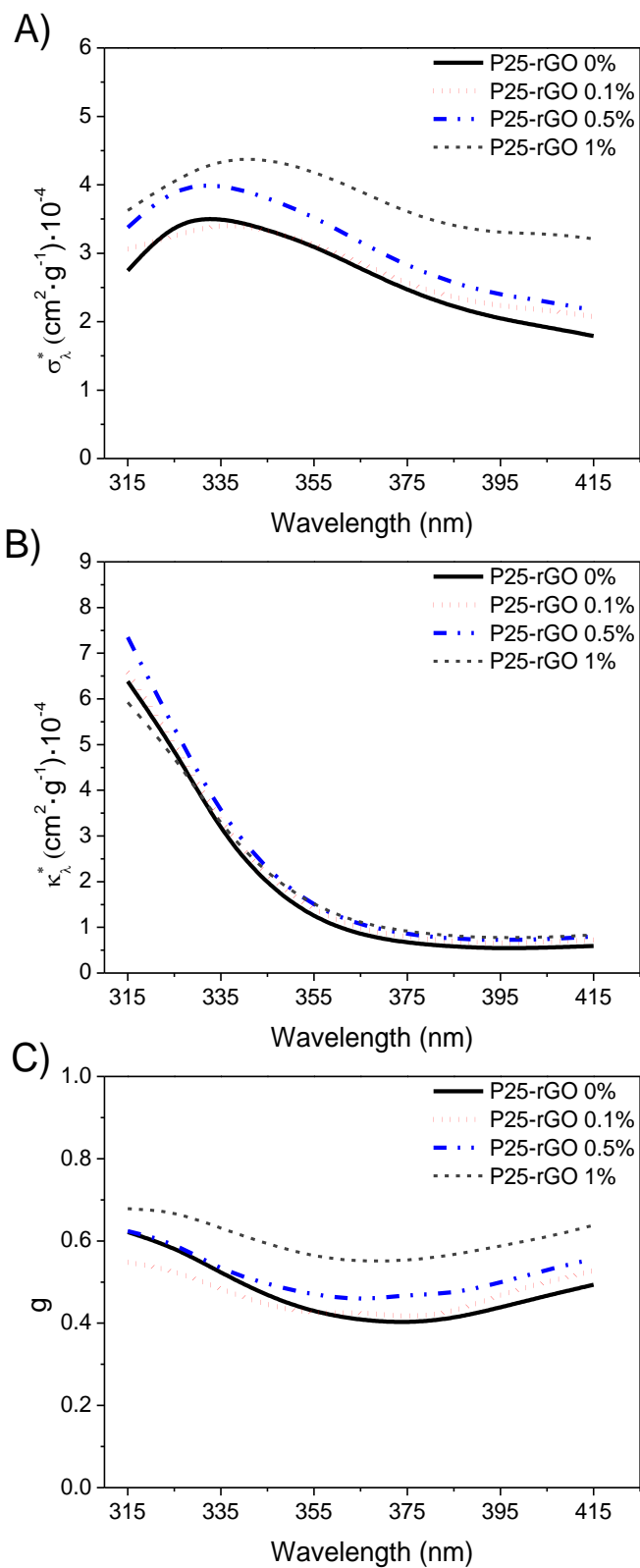


Figures 5. SEM images of P25-rGO 0% (a) and P25-rGO 1% (b).
EDX profile of P25-rGO 1% photocatalyst (c).

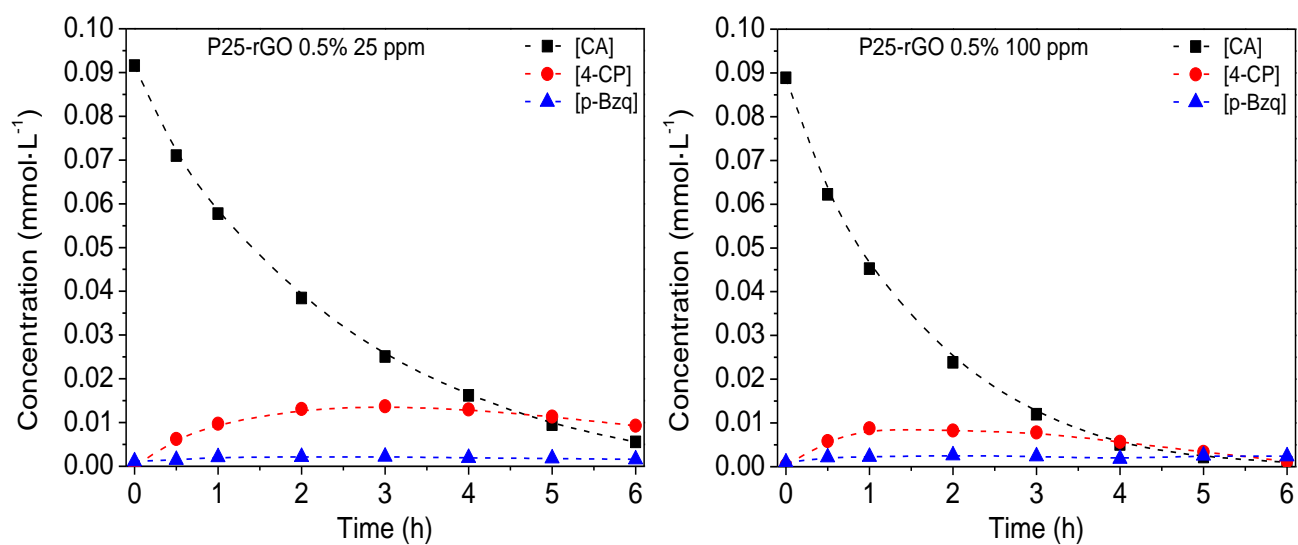


Figures 6. TEM images of P25-rGO photocatalysts.

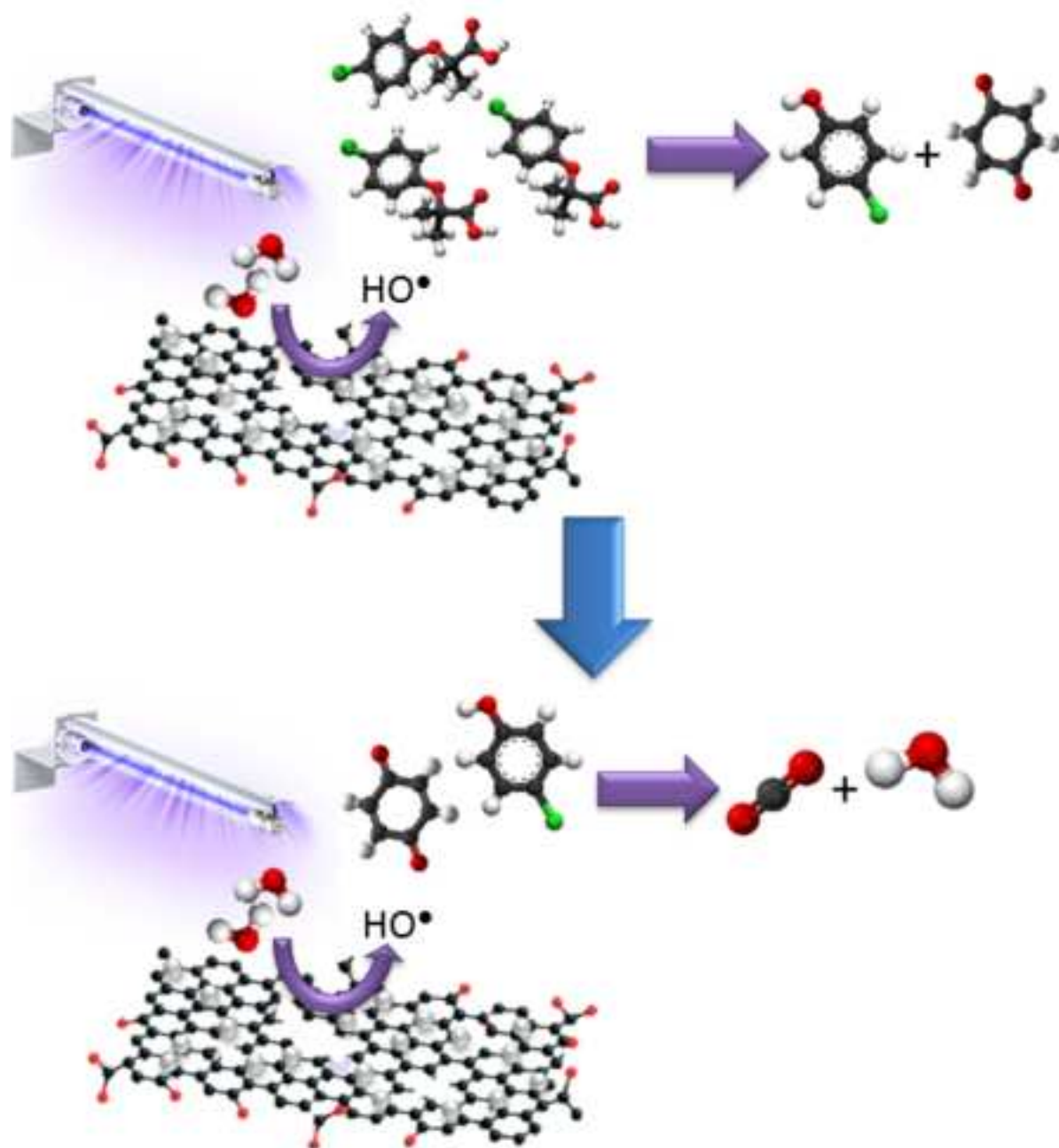
(a) P25-rGO 0%; (b) HRTEM micrograph of the TiO_2 particles and the inset shows the Fast Fourier transform (FFT) pattern; (c) and (d-f) are TEM and HRTEM images of P25-rGO 1%, respectively.



Figures 7. Optical properties of the different TiO₂-rGO photocatalysts: (A), specific scattering coefficient (σ_{λ}); (B), specific absorption coefficient (κ_{λ}); (C), asymmetry factor (g_{λ}).



Figures 8. Evolution of clofibric acid (CA) concentration and the main intermediates, 4-chlorophenol (4-CP) and p-benzoquinone (p-Bzq), with 25 and 100 mg·L⁻¹ of P25-rGO 0.5%.



Highlights

- TiO_2 -rGO optical properties were estimated using the Monte Carlo method
- TiO_2 -rGO exhibited higher scattering coefficients than TiO_2
- rGO was found to increase quantum efficiency of bare TiO_2
- Complete degradation of clofibric acid was achieved after 6 h of irradiation time

Supplementary Material

[Click here to download Supplementary Material: Supporting Information.docx](#)